Published in: The Journal of Physical Chemistry C. 2013, 117(12): 6126-6135. doi:10.1021/jp308941g

The role of TiO_2-doping on RuO_2 coated electrodes for the water oxidation reaction

*Lars-Åke Näslund**[,†,‡], *Carlos. M. Sánchez-Sánchez*[§], *Árni S. Ingason*[‡], *Joakim Bäckström*[†,#], *Enrique Herrero*[§], *Johanna Rosen*[‡], *and Susanne Holmin*[†]

[†]Permascand AB, SE-840 10 Ljungaverk, Sweden

[‡]Department of Physics, Chemistry, and Biology (IFM), Linköping University, SE-58183 Linköping, Sweden

[§]Instituto Universitario de Electroquímica, Universidad de Alicante, Ap. 99, ES-03080 Alicante, Spain

KEYWORDS: Mixed oxide coating, Electrocatalysis, Oxygen evolution reaction, Charge transfer, Scanning electrochemical microscopy, X-ray photoelectron spectroscopy.

ABSTRACT: Electrochemical water splitting into H_2 and O_2 presents a significant and challenging energy loss due to the high overpotential required at the anode. Today, in industrially relevant applications, dimensionally stable anodes (DSA®) based on the electrocatalytic active RuO_2 are conventionally utilized. To enhance the resistance against corrosion, incorporation of TiO_2 in the RuO_2 coated electrodes is widely employed. In the present work we have used scanning electrochemical microscopy (SECM) to demonstrate that TiO_2-doped RuO_2 coated

electrodes, in addition to being more durable, also show an electrocatalytic activity that is, on average, 13% higher as compared to the pure RuO_2 coated electrodes. We also demonstrate that cracks in the pure RuO_2 coating are the most active zones, probably because Ti from the Ti support has diffused into the first applied layer of the RuO_2 coating. To reveal the nature of this enhanced activity for water oxidation displayed on TiO_2-doped RuO_2 electrodes we have employed X-ray photoelectron spectroscopy (XPS) for material characterization. The results show that the electrocatalytic activity enhancement displayed on the mixed $(Ru_{1-x}:Ti_x)O_2$ coating is promoted through a charge transfer from the RuO_2 to the TiO_2, which provides new and more reactive sites designated as activated $RuO_2^{\delta+}$.

1. INTRODUCTION

Dimensionally stable anodes (DSA®) are functionalized anodes that can be composed of various types of catalyst coatings and are widely employed in a large variety of industrial electrochemical processes, e.g., chlor-alkali and chlorate processes, water treatment, electrowinning, and water electrolysis.[1,2] These anodes are typically made of titanium (Ti) coated with a platinum-group metal oxide where the choice of one or several metal oxides is made on the basis of the actual targeted process. Among the different processes where DSA® electrodes are utilized the water electrolysis process, either in acidic or alkaline media, represents a promising candidate for a convenient route for energy storage and conversion. However, electrochemical water splitting into hydrogen (H_2) and oxygen (O_2) suffers from a significant and challenging energy loss due to the high overpotential required at the anode in order to carry out the water oxidation reaction and efficiently produce oxygen evolution.[3,4] Although conventional material supports, such as carbon black, have been investigated, their low resistance against corrosion at high anodic potentials have made other materials such as titanium dioxide (TiO_2),

oxygen deficient Magnéli phases Ti_nO_{2n-1}[5] or Sb-doped SnO_2[6] more convenient. Other approaches have, however, also been proposed in the literature, such as freely diffusing iridium oxide (IrO_2) nanoparticles as redox catalyst that impact the substrate electrode by stirring the solution.[7] In that case, water oxidation in alkaline aqueous solution is achieved at an overpotential of 0.29 V with a 100% current efficiency. Nevertheless, with todays constantly increasing energy costs, the depletion of fossil fuel reserves, and the negative impact of greenhouse effect gases, industrial applications demand highly efficient and inexpensive to produce DSA® electrodes with low overpotentials for, e.g., the electrocatalytic water oxidation and with better selectivity against unwanted processes. Most DSA® electrodes for water oxidation are therefore designed with an electrocatalytic coating of metal oxide nanoparticles, typically including ruthenium dioxide (RuO_2) and/or IrO_2, which are deposited through thermal decomposition of metal salt solutions on a conductive metal substrate electrode.[8]

In particular, RuO_2 exhibits high catalytic performance for water oxidation with a moderate overpotential and RuO_2 coated electrodes are, thus, one of the most studied catalytic metal oxides for the oxygen evolution reaction (OER).[9-17] Moreover, RuO_2 exhibits various interesting properties such as metallic conductivity, low resistivity (3-5 10^{-5} Ω cm[18]), high thermal stability, and high resistance to chemical corrosion, which provides reasonable long-term stability.[1,2] The reaction scheme for the water oxidation reaction on RuO_2 in acidic media occurs by reacting RuO_2 with water and forming the unstable RuO_3, as an intermediate, that subsequently decomposes into O_2 and RuO_2, regenerating the electrode material.[9] Hence, RuO_2-based electrodes belong to the group of anodes that undergo changes in their metal oxidation state when electrochemically active. Although, the complete reaction scheme includes many different

reaction steps, see e.g. ref. 14, we will in this work, for simplicity, only consider the two main parts represented by reactions (1) and (2):

$$2RuO_2 + 2H_2O \rightarrow 2RuO_3 + 4H^+ + 4e^- \quad (1)$$

$$2RuO_3 \rightarrow 2RuO_2 + O_2 \quad (2)$$

Designing the functionality of a RuO_2 thin film toward improved water oxidation activity may, however, require mixing with other metal oxides, which in most cases also form structures not too different from the tetragonal rutile phase of RuO_2. The presence of an additional metal oxide in the RuO_2 film may sometimes come from the oxidation of the material support. Then, because Ti usually is the substrate material for coated DSA® electrodes, the most common additional metal oxide is TiO_2. Despite the well known fact that rutile TiO_2 presents semiconductor properties with a band gap of 3 eV, a prototypical DSA®, with a composition close to $(Ru_{0.3}:Ti_{0.7})O_2$, conducts electricity very efficiently and provides profitable high electrocatalytic activity. The main arguments for a mixed $(Ru_{1-x}:Ti_x)O_2$ coating are a more stable and a less expensive DSA® coating compared to a pure RuO_2 coating.[2] The higher activity than expected on the mixed $(Ru_{1-x}:Ti_x)O_2$ coating is, however, still puzzling and other studies have, in addition, showed a Ti-enrichment on the surface of the mixed $(Ru_{1-x}:Ti_x)O_2$ coatings.[19-21] The question that arises is: does TiO_2 actively contribute to improve the electrocatalytic activity of the RuO_2 coating for the process of relevance?

The aim of the present work is to answer the question if TiO_2 is a passive or active component for the electrocatalytic water oxidation on $(Ru_{1-x}:Ti_x)O_2$ electrodes in acidic aqueous solution by providing additional insight into the reaction mechanism. For this reason, we have studied the

mixed $(Ru_{1-x}:Ti_x)O_2$ and the pure RuO_2 coatings through a compelling electrochemical probe technique known as the scanning electrochemical microscopy (SECM)[22] complemented with the chemically sensitive X-ray photoelectron spectroscopy (XPS), which is extensively used for material characterization.[23] The SECM has been proposed as an analytical tool for exploring the electrocatalytic activity of different materials, such as metallic nanoparticles[24,25] and metal oxides.[26] In particular, the substrate generation–tip collection (SG/TC) mode of the SECM[27] has recently been proved as a useful tool for visualizing the chlorine evolution at DSA® electrodes in highly concentrated brine solutions[28] and previously the OER at micro-sized Ir/Sn binary oxides using a shielded tip[26]. In the present work we use the SG/TC mode of the SECM for comparing the electrocatalytic activity for water oxidation displayed at TiO_2-doped and un-doped DSA®-like RuO_2 based electrodes. On the one hand, the SECM provides an overview image of the electrochemical activity at the two tested coatings,[29,30] and on the other hand, the conventional XPS, as well as the higher resolution synchrotron radiation based XPS, provide element-specific information of the electronic structure of the probed components in the tested electrode areas,[23] which provide complementary information to reach a better understanding of the electrocatalytic reaction mechanism.

2. EXPERIMENTAL SECTION

2.1. Sample Preparation. Samples of RuO_2-, TiO_2-, and mixed $(Ru_{1-x}:Ti_x)O_2$ coatings were prepared on commercially pure titanium (grade 2) metal sheets 100 x 100 x 0.5 and 45 x 28 x 1 mm^3 for the XPS- and SECM samples, respectively. Before use all Ti sheets were degreased and rinsed in deionized water. In addition, the Ti sheets for the XPS samples were pickled for 20 minutes in boiling 18% HCl(aq) to remove the oxide layer before the first application of the

precursor solutions. All coatings, except the TiO_2 for the SECM samples, were prepared by a conventional multi-step precursor solution application/calcination method. This procedure was repeated several times to obtain superimposed layers of the corresponding metal oxide. The precursor solutions were applied onto the Ti sheets with carefully pre-wetted brushes and subsequently heat treated in air for 10 minutes at 80 °C followed by 10 minutes calcinations at 470 °C. The coating procedure was repeated five times to achieve a coating thickness of 3 µm. For the XPS samples the heat treatment at 470 °C was prolonged to 1 h after the fifth application. The TiO_2 on the SECM samples were formed spontaneously on the available bare titanium zones during the heat treatment in air.

The precursor solutions for the XPS- and SECM samples were prepared according to two different recipes where the former corresponded to an industrial standard recipe while the latter required precursor solutions with lesser tendencies to spread over the Ti sheets. The latter recipe was necessary in order to allow a narrow coating free zone of ~1.5 mm width in between the RuO_2 coating and the mixed $(Ru_{1-x}:Ti_x)O_2$ coating since they are both applied on the same Ti sheet. The narrow zone of bare titanium becomes TiO_2 after the calcination treatment and is useful for clearly separating the two Ru-based coatings at the SECM measurements. All Ru precursor solutions were prepared from $RuCl_3 \times nH_2O$ salt from Heraeus, (40.27 wt-% Ru, analytical reagent grade) while the Ti precursor solutions were prepared from commercially available acidic $TiCl_3$-solution from UTS Scandinavia, containing 5.2 wt-% Ti in 15 wt-% HCl, and Alfa Aesar, containing 6.1 wt-% Ti in 3 wt-% HCl, for the XPS- and the SECM samples, respectively. The solvents were 15 wt-% HCl + isopropanol for the XPS samples and 1-propanol for the SECM samples. The preparations of the precursor solutions are summarized in Table 1.

The *x*-value in the mixed $(Ru_{1-x}:Ti_x)O_2$ coatings were 0.50 and 0.70 for the XPS samples and 0.24 for the SECM samples. Bulk- *versus* surface sensitive XPS measurements, however, indicates that there is a Ti enrichment at the surface of the mixed $(Ru_{1-x}:Ti_x)O_2$ coatings and for the SECM sample, due to the selection of solvent, the Ti enrichment is significant. For that reason a precursor solution that contains 76% Ru (24% Ti) was necessary to obtain a surface composition with a Ru:Ti ratio similar as the XPS sample with the mixed $(Ru_{0.5}:Ti_{0.5})O_2$ coating. Although the surface composition of the mixed $(Ru_{1-x}:Ti_x)O_2$ coating for the SECM sample has the *x*-value close to 0.5 we will use the Ru:Ti ratio in the precursor solution, i.e. *x*-value 0.24, throughout the text.

Table 1. Chemicals, quantity and solvents used for the Ru- and Ti precursor solutions

Sample[a]	Precursor solution	Chemicals[b]	Quantity	Solvent[c]	Final Volume
RuO_2	Ru	$RuCl_3$ x nH_2O (salt)	15.78 g	2.85 ml 2-propanol + 15 wt-% HCl	50 ml
TiO_2	Ti	5.2 wt-% Ti in 15 wt-% HCl	115.7 g	5.7 ml 2-propanol + 15 wt-% HCl	100 ml
$(Ru_{0.5}:Ti_{0.5})O_2$	Ru + Ti, (50:50)	Ru precursor solution Ti precursor solution	10 ml 10 ml		20 ml
$(Ru_{0.3}:Ti_{0.7})O_2$	Ru + Ti, (30:70)	Ru precursor solution Ti precursor solution	7.5 ml 17.5 ml		25 ml
RuO_2	Ru	$RuCl_3$ x nH_2O (salt)	15.73 g	1-propanol	50 ml
$(Ru_{0.76}:Ti_{0.24})O_2$	Ru + Ti, (76:24)	$RuCl_3$ x nH_2O (salt) 6.1 wt-% Ti in 3 wt-% HCl	7.86 g 7.50 g	1-propanol	50 ml

[a]The first four samples were prepared for the XPS measurements and the last two for the SECM measurements.

[b]The chemicals were of analytical reagent grade obtained from Heraeus ($RuCl_3$ x nH_2O), UTS Scandinavia (5.2 wt-% Ti in 15 wt-% HCl), and Alfa Aesar (6.1 wt-% Ti in 3 wt-% HCl).

[c]The solvents were of analytical reagent grade obtained from Lab-Scan.

2.2. Scanning Electrochemical Microscopy. The SECM images were acquired at room temperature using the SG/TC mode on a CHI 910B microscope (CH Instruments) in a four-electrode configuration. The electrochemical cell was built in Teflon with an 8 mm diameter aperture. The substrate electrode simultaneously, but separately, displayed three different oxide coatings; $(Ru_{0.76}:Ti_{0.24})O_2$ / TiO_2 / RuO_2. This substrate electrode plate was tightened at the bottom of the Teflon cell via an O-ring allowing a portion of the three different oxide coatings to be in contact with the electrolyte. A 100 μm diameter gold ultramicroelectrode (UME) was employed as a probe electrode for sensing the O_2 generated on the substrate electrode. This tip was built by heat-sealing, under vacuum, a gold wire (Goodfellow, 99.99% purity) in a borosilicate glass capillary. After this, the capillary glass was polished to reveal the gold surface and sharpened using sand paper and different alumina powders to yield a flat disk.[22] The usual parameters to define a SECM tip are the tip radius (a), the tip radius including the glass sheath (rg), the RG value ($RG = rg/a$), and the normalized distance ($L = d/a$), where d is the tip-substrate electrode distance. The gold tip used for the SECM imaging presented a = 50 μm and RG = 10.

Three different zones, $(Ru_{0.76}:Ti_{0.24})O_2$, TiO_2, and RuO_2, respectively, could be distinguished on the substrate electrode surface scanned by the SECM tip. The whole substrate electrode area was 45 x 28 mm^2, but the Teflon cell only allows an available area in contact with the solution of 50 mm^2.

For SECM imaging, the gold tip was located at a constant tip-substrate electrode distance (d = 30 μm) and its potential was held constant at -0.05 V in a 0.1 M $HClO_4$ solution without purging the oxygen from the air. The potential applied to the substrate electrode was kept constant at 1.35

V: more positive values produce the formation of too many O_2 bubbles that may interfere the image collection. An SECM image represents the oxygen reduction current collected at the tip electrode meanwhile this tip was scanned in the xy-plane above the substrate electrode. The tilt of this setup was $\Delta z/\Delta x$ ($\Delta z/\Delta y$) ≤ 8 μm/mm. A homemade reversible hydrogen electrode (RHE) filled with 0.1 M $HClO_4$ solution was used as the reference electrode and it was assembled before each trial as described elsewhere.[31] The potential of this RHE remained stable during the entire experimental time period. All potentials in the text are reported with respect to the RHE. A gold wire, 0.5 mm in diameter, was used as a counter electrode.

2.3. X-ray Diffraction. The conventional multi-step precursor solution application/calcination method produces coatings that are built up by nanoparticles.[32] To determine the size of the nanoparticles X-ray diffraction (XRD) measurements were performed with a Panalytical Empyrean MRD system, using Ni-filtered Cu K_α radiation. Symmetric 2Θ-Θ scans were performed using line focus and an X-ray mirror on the incident side and a collimator on the diffracted side. To compare the particle size between the two samples the Scherrer equation was used[33,34] with the shape factor K = 0.9 and the full width of half maximum (fwhm) of the RuO_2 (110) reflection. This will give an underestimation of the particle size, since other line-broadening effects are neglected, but the relative sizes should be correct for the two cases of RuO_2-, and mixed $(Ru_{1-x}:Ti_x)O_2$ coatings.

2.4. X-ray Photoelectron Spectroscopy. The monochromatic Al K_α (1486.6 eV) irradiation based XPS was acquired using a Gammadata Scienta Esca-200 with a total energy resolution for the spectroscopy near 0.36 eV. The X-ray incident angle was 45° providing a spot size on the sample that was 80 x 2500 μm^2. The probing depth was estimated to be around 20 Å.[35,36]

The synchrotron radiation based hard X-ray photoelectron spectroscopy (HAXPES) were acquired at the undulator beamline 47XU, SPring-8, Japan, using a Gammadata Scienta R4000 electron energy analyzer with a total energy resolution for the spectroscopy better than 0.28 eV at an incident photon energy of 7940.1 eV. The X-ray incident angle was 1° providing a spot size on the sample that corresponds to 43 x 3225 μm^2 in vertical and horizontal direction, respectively. The probing depth was estimated to be around 70 Å.[35,36]

The binding energy scale of all XPS spectra presented here were calibrated against the Fermi-edge (E_f) of a gold (Au) reference, which was set to a binding energy of 0 eV. No indications of charging of the samples were observed. Normalization of all spectra was performed at the background on the low binding energy side of the main peak/peaks.

3. RESULTS AND DISCUSSIONS

3.1 Optical and SECM SG/TC imaging. The optical microscopy (Zeiss Axiotech Vario) image displayed in the upper panel of Figure 1 shows a SECM sample where the three different coating zones of mixed $(Ru_{0.76}:Ti_{0.24})O_2$ (left), TiO_2 (middle), and the RuO_2 (right), respectively, all applied on the same Ti sheet, easily can be distinguished. The two Ru-based coatings are built up by spherical nanoparticles[32] and through XRD the average particle sizes were determined to be 7.0 and 7.3 nm for the mixed $(Ru_{0.76}:Ti_{0.24})O_2$ coating and the RuO_2 coating, respectively. Since the size determination of the nanoparticles is an indirect estimation of the total surface area[34] the XRD measurements indicate that the two coatings present equally large total surface area and the number of active sites should be, as a first approximation, proportional to the Ru-content. However, while the mixed $(Ru_{0.76}:Ti_{0.24})O_2$ coating is homogeneous, on the length scale shown in the optical image, the RuO_2 coating, on the contrary, shows cracks that mainly are

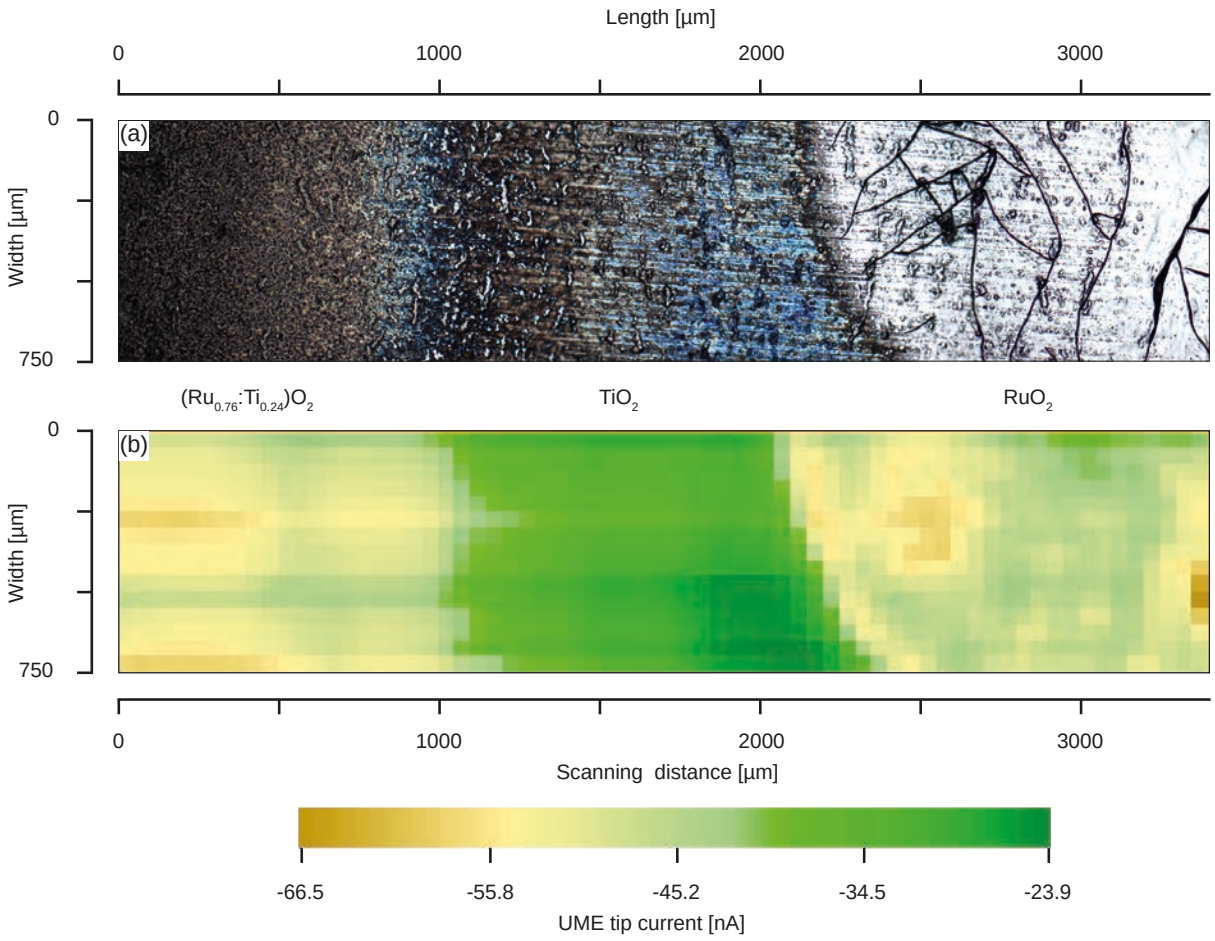

Figure 1. Optical- and scanning electrochemical microscopy are shown in the upper and lower panel as part (a) and (b), respectively. The SECM SG/TC image displays the UME tip current collected from the OER activity on the substrate electrode composed simultaneously by the two oxide coatings $(Ru_{0.76}:Ti_{0.24})O_2$ and RuO_2 separated by TiO_2. Tip and substrate potentials held constant at -0.05 V and 1.35 V *versus* RHE, respectively, in a 0.1 M $HClO_4$ solution without purging the oxygen from the air. Tip–substrate distance = 30 µm. Scan rate = 50 µm s^{-1}. The mixed $(Ru_{0.76}:Ti_{0.24})O_2$ coating shows an even distribution of moderate to high OER activity over the whole probed area. The RuO_2 coating, on the other hand, shows two small but very active areas separated by a large region with low to moderate OER activity.

5-15 μm wide: one crack on the far right corner of Figure 1, part (a), shows the largest width of 32 μm.

The lower panel of Figure 1 shows the SECM SG/TC image obtained when the gold UME tip was sensing the electrochemical activity as it was scanned over the sample surface, i.e. revealing where the oxygen evolution reaction was occurring on the substrate electrode. The dark green and brown areas correspond to low and high current collected on the UME tip, respectively, representing the activity for water oxidation displayed by the three different coatings present on the substrate electrode. Since the probed area for the SECM is the same as shown in the optical microscope image, all three different coatings are present; the mixed $(Ru_{0.76}:Ti_{0.24})O_2$ (left) and the RuO_2 (right) separated by TiO_2 (middle). Figure 1, part (b), clearly shows that only the Ru-based coatings present high catalytic activity for OER, since the tip current on the TiO_2 zone presents the lowest value in the image. The striking observation is, however, that the left side of the image shows an average higher current and a more evenly distributed electrocatalytic activity than the right side, i.e. the $(Ru_{0.76}:Ti_{0.24})O_2$ coating is more efficient for water oxidation and O_2 production than the pure RuO_2 coating.

The average UME tip current collected per surface area of the mixed $(Ru_{0.76}:Ti_{0.24})O_2$ coating and the RuO_2 coating are -20.7 and -19.9 $pA/\mu m^2$, respectively. If the average current per surface area of the TiO_2 film between the coatings, -13.7 $pA/\mu m^2$, is regarded as the background signal of the SECM measurement, i.e. the electrochemical current provided at the tip by the oxygen initially present in the air saturated acid solution, then the average current per surface area originated from the OER activity on the mixed $(Ru_{0.76}:Ti_{0.24})O_2$ coating and the RuO_2 coating correspond to -7.0 and -6.2 $pA/\mu m^2$, respectively. The electrocatalytic OER activity is, thus, about 13% higher for the mixed $(Ru_{0.76}:Ti_{0.24})O_2$ coating, compare to the RuO_2 coating, despite

the fact that the average particle size of both coatings are very similar and the former coating has a significant lower RuO_2 content.

The OER activity displayed on the RuO_2 coating area is, however, non-uniform and the upper left section and the area close to the border to the TiO_2 film show higher OER activity as compared to the middle section of the same coating. The average current per surface area of the high active region in the upper left section of the RuO_2 coatings is -23.0 pA/μm^2, which can be compared to the low active region in the low left and middle sections with an average current per surface area of -19.4 pA/μm^2. Subtracting the background contribution leads to an OER activity that corresponds to -9.3 and -5.7 pA/μm^2 for the high and low active sections, respectively. The low OER activity region on the RuO_2 coating is, thus, about 61% of the high OER activity region at the upper left section of the same RuO_2 coating and about 81% of the activity displayed at the mixed $(Ru_{0.76}:Ti_{0.24})O_2$ coating.

In addition to the high activity in the upper left section of the RuO_2 coating and in the area close to the border to the TiO_2 film, the low left and middle section of the RuO_2 coating has variations in form of higher activity in near vertical bands across the coating. The origin of those bands can be correlated with the crack pattern displayed for RuO_2 in Figure 1, part (a), which is shown in the upper panel of Figure 2: the SECM image that corresponds to the RuO_2 coating region of the substrate electrode is superimposed over the crack pattern on the RuO_2 coating shown in the optical microscopy image. The comparison clearly points out that higher OER activity is displayed in the close vicinity of the cracks in the RuO_2 coating. Figure 2, part (b), shows, for the RuO_2 coating, the tip current profile extracted from the SECM image for one single scan line with the crack pattern for this single line superimposed on it. Although the widths of the cracks are much smaller than the UME tip diameter, 5-15 μm and 100 μm,

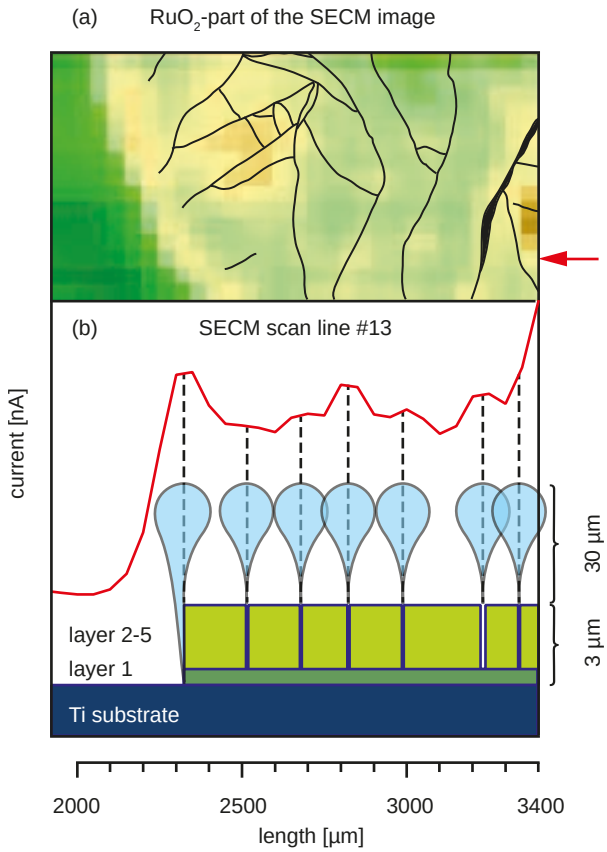

Figure 2. (a) Comparison between the SECM image and the cracks observed in the optical microscope image reveals enhanced OER activity at the cracks in the RuO_2 coating. (b) The current profile at SECM scan no. 13, indicated with an arrow in the SECM image in (a), compared with the crack location. Although the small width of the cracks (5-15 µm) the plume of oxygen gas leaving the cracks in the RuO_2 coating will have a size comparable with the UME diameter of 100 µm.

respectively, and therefore should not be noticeable in the SECM image, the O_2 gas formation in the cracks of the RuO_2 coating will rise and spread out like a plume when the O_2 bubbles leave the cracks, allowing the 100 µm UME tip to sense the O_2 concentration variation when it is above the cracked RuO_2. We can therefore suspect that the cracks are even more active, compare to the RuO_2 coating in between them, than the SECM image shows. The observation of higher

OER activity at the cracks and at the border to the TiO_2 film suggests that an enhanced OER activity occurs where Ti has diffused into the RuO_2 coating, i.e. close to the TiO_2 film border and where the cracks have penetrated down to the first applied layer, see Figure 2, part (b): the Ru precursor solution is corrosive and leaches out Ti from the Ti sheet that diffuses into the first applied layer. The OER activity is, thus, proportional to the crack density, which is apparent at the upper left section of the RuO_2 coating where the crack density is as largest. At the border to the TiO_2 film the 1st layer of the RuO_2 coating is exposed, see Figure 2, part (b), and the OER activity is, thus, enhanced: as a comparison we can see the opposite effect at the mixed $(Ru_{0.76}:Ti_{0.24})O_2$ coating, i.e. a reduced activity at the border to the TiO_2 film compare to the remaining part of the coating.

3.2. X-ray Photoelectron Spectroscopy. From the SECM results we can conclude that TiO_2-doping plays a significant role in enhancing the water oxidation activity on the RuO_2 coatings. As TiO_2 is known to be a poor catalyst for the OER,[14,37] see also middle section of the SECM image in Figure 1, the enhanced activity must be due to an interaction between the Ti and the Ru in the mixed oxide coating. To reveal the nature of this interaction we have employed an element selective and environmentally sensitive X-ray based technique using both conventional and synchrotron radiation. Figure 3 presents the binding energy region for the Ti 2p, which coincide with the Ru $3p_{3/2}$ peak, as obtained with HAXPES for the three different coating electrodes. The Ti 2p spectrum of the pure TiO_2 coating, part (a), shows the Ti $2p_{3/2}$ and Ti $2p_{1/2}$ peaks located at 459.3 and 465.0 eV, respectively, the pure RuO_2 coating, part (b), displays a broad Ru $3p_{3/2}$ at 462.4 eV, and the mixed $(Ru_{0.5}:Ti_{0.5})O_2$ coating, part (c), shows the broad Ru $3p_{3/2}$ superimposed between the Ti $2p_{3/2}$ and Ti $2p_{1/2}$ peaks. As shown in Figure 3, the HAXPES spectrum of the mixed $(Ru_{0.5}:Ti_{0.5})O_2$ coating displays a 0.3 eV shift of the Ti 2p toward lower binding energies,

which suggests that the Ti-atoms in the mixed $(Ru_{0.5}:Ti_{0.5})O_2$ coating have gained charge compared to the Ti-atoms in the pure TiO_2 coating.[38-40]

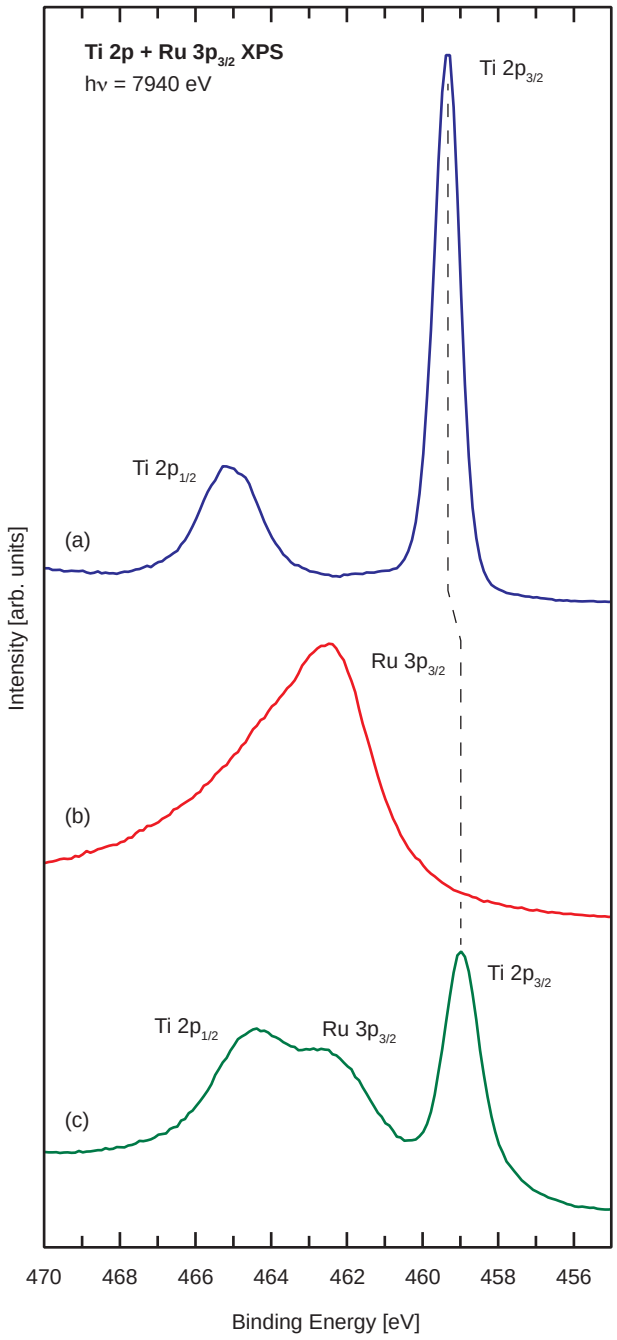

Figure 3. Ti 2p + Ru $3p_{3/2}$ XPS of (a) TiO_2-, (b) RuO_2-, and (c) mixed $(Ru_{0.5}:Ti_{0.5})O_2$ coatings obtained through hard X-ray excitation. The Ti $2p_{3/2}$ peak for the mixed $(Ru_{0.5}:Ti_{0.5})O_2$ coating shows a 0.3 eV shift toward lower binding energy compare to the pure TiO_2 coating.

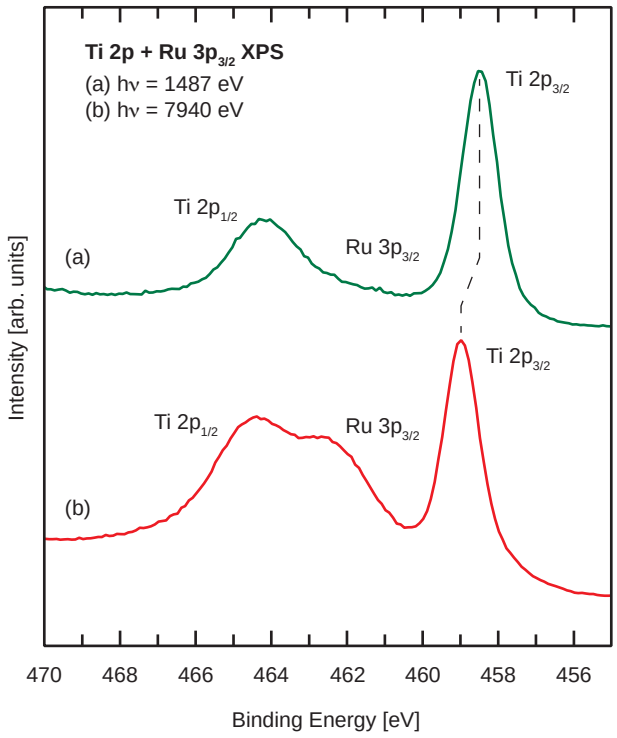

Figure 4. Ti 2p + Ru $3p_{3/2}$ XPS of mixed $(Ru_{0.5}:Ti_{0.5})O_2$ obtained through (a) 1.49 keV and (b) 7.94 keV excitation energy. The intensity of the Ru $3p_{3/2}$ peak is much lower when using the surface sensitive excitation energy, suggesting significant Ti segregation to the surface region. The probing depths were estimated to be 20 and 70 Å, respectively.[35,36]

A comparison between conventional Al K_α XPS and synchrotron radiation based HAXPES of the mixed $(Ru_{0.5}:Ti_{0.5})O_2$ coating, recorded on the same sample, is displayed in Figure 4. As the intensity of the Ru $3p_{3/2}$ component at the surface sensitive XPS spectrum, part (a), is much less than the corresponding peak in the deep probing HAXPES spectrum, part (b), the comparison clearly shows that Ti has segregated to the surface. The comparison further shows a larger Ti 2p shift of the surface sensitive XPS spectrum, which is a consequence of the Ti segregation since the shift of the Ti 2p becomes larger when the amount of TiO_2 increases as shown in Figure 5.

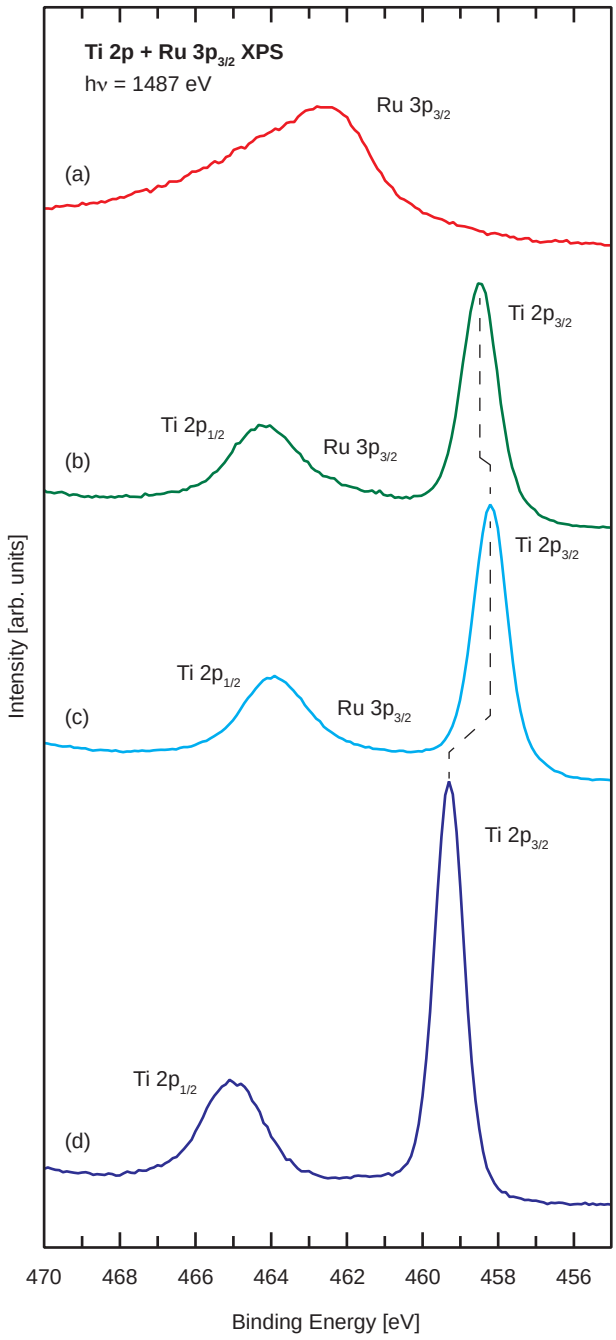

Figure 5. Ti 2p + Ru $3p_{3/2}$ XPS of (a) pure RuO_2-, (b) mixed $(Ru_{0.5}:Ti_{0.5})O_2$-, (c) mixed $(Ru_{0.3}:Ti_{0.7})O_2$-, and (d) pure TiO_2 coatings obtained through soft X-ray excitation. The Ti $2p_{3/2}$ peak shift toward lower binding energies suggests a gain in charge and is sensitive to the amount of RuO_2 in the coating.

Figure 5 presents Al K_α XPS spectra of Ti 2p + Ru $3p_{3/2}$ for mixed $(Ru_{1-x}:Ti_x)O_2$ coatings where x = 0, 0.5, 0.7, and 1: the value of x represents the Ru:Ti ratio in the precursor solution and not necessary the true fraction of Ti at the surface of the coatings. The observed Ti $2p_{3/2}$ peak positions displayed in Figure 5 are shown in Table 2. The shift of the Ti $2p_{3/2}$ peak toward lower binding energies suggests that the Ti atoms in the mixed $(Ru_{1-x}:Ti_x)O_2$ coatings have gained charge and the extent of the charge transfer is sensitive to the amount of RuO_2 in the coating. For the mixed $(Ru_{0.3}:Ti_{0.7})O_2$ coating the Ti $2p_{3/2}$ peak is shifted to 458.2 eV, which is a charge transfer half as much required to transform Ti^{4+} into Ti^{3+}: the Ti $2p_{3/2}$ peak for Ti^{3+}, i.e. titanium(III)oxide, appears around 457.2 eV.[41] Figure 5 further indicates that the charge transfer to Ti increases with lower Ru content in the mixed $(Ru_{1-x}:Ti_x)O_2$ coatings, maybe because a smaller amount of Ru atoms in the mixed metal oxide nanoparticles cannot withstand the Ti atoms large appeal for electrons. A similar observation is reported from a study of gold (Au) nanoparticles on TiO_2 where a charge transfer from Au to TiO_2 occurs when the Au nanoparticle size is below 5 nm and increases significantly at Au nanoparticle sizes below 2 nm.[42] A relevant question is whether the corresponding shift toward higher binding energies can be observed for the Ru 3d peaks.

Table 2. Ti $2p_{3/2}$ peak positions for $(Ru_{1-x}:Ti_x)O_2$ coatings

Sample	Binding energy [eV]
TiO_2	459.3
$(Ru_{0.3}:Ti_{0.7})O_2$	458.2
$(Ru_{0.5}:Ti_{0.5})O_2$	458.4
Titanium(III)oxid	457.2[a]

[a]Peak position obtained from ref.[41]

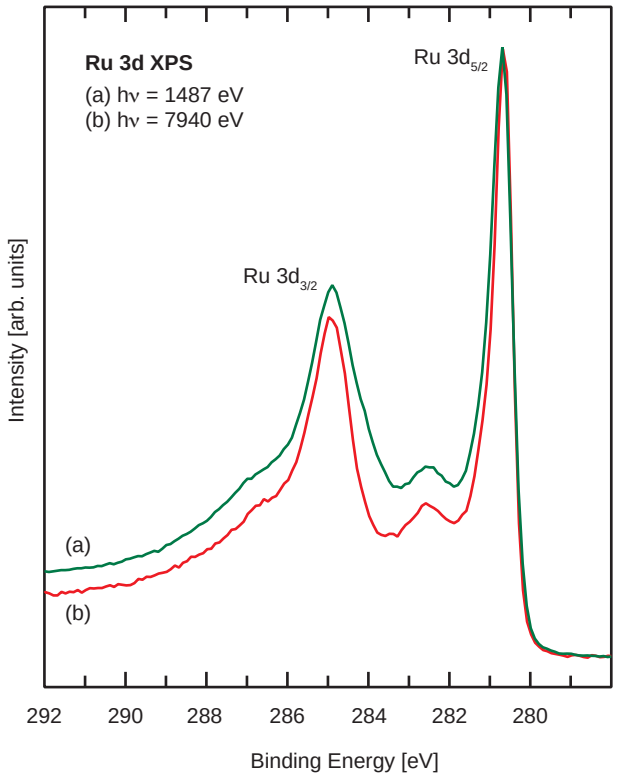

Figure 6. Ru 3d spectra of polycrystalline RuO_2 obtained through (a) soft- and (b) hard X-ray photoelectron spectroscopy. The comparison shows that an excitation energy of 1.49 keV, which is surface sensitive, generates a Ru 3d spectrum with identical features as a Ru 3d spectrum obtained through excitation energy of 7.94 keV, which is bulk sensitive. The probing depths were estimated to be 20 and 70 Å, respectively.[35,36]

Characterization of RuO_2 coatings through XPS has been performed previously.[43-46] The X-ray sources have in all cases been either an Mg or Al anode providing photons at 1.25 keV and 1.49 keV, respectively. An example of a Ru 3d XPS spectrum, obtained using excitation energy 1.49 keV, is shown in Figure 6, part (a). Although the binding energy region of Ru 3d coincide with the C 1s, the XPS spectrum in Figure 6 resembles a corresponding XPS spectrum of RuO_2(110) grown in vacuum on TiO_2(110)[47] and, thus, indicates very small contribution from C-

contaminations. Included in Figure 6, as part (b), is also a Ru 3d XPS spectrum obtained using monochromatized synchrotron radiation of 7.94 keV. Except from a slightly better resolution, 0.28 eV for part (b) compare to 0.36 eV for part (a), and different background contribution, the two spectra are very similar and we can therefore conclude that the Ru 3d spectra in Figure 6 show no significant amount of C 1s intensity superimposed on the Ru 3d spectra. This conclusion is further supported through peak fitting of the Ru 3d XPS spectrum, presented in the Supporting Information, where the peak fitting procedure, which included plausible C-contaminations, suppressed the C 1s components down to zero intensity.

The Ru 3d XPS spectrum features the primary spin-orbit components $3d_{3/2}$ and $3d_{5/2}$ at 284.9 and 280.7 eV binding energies, respectively. The fwhm for the Ru $3d_{5/2}$ peak in Figure 6, part (b), is about 0.6 eV, while the corresponding Ru $3d_{3/2}$ peak shows a larger fwhm, about 1.2 eV, due to Coster-Kronig broadening:[48] an $M_4M_5N_{45}$ Coster-Kronig decay channel reduces the lifetime of the Ru $3d_{3/2}$ hole state and thereof an increased core hole lifetime broadening of the Ru $3d_{3/2}$ peak.

In addition to the dominant low binding energy spin orbit doublet there are two satellites at 282.5 and 286.8 eV, respectively, whose origin is debated in the literature. Some authors suggest that they originate from a RuO_3 component in the film[43,45] while others propose that they are due to surface atoms, e.g. the fivefold-coordinated Ru-atoms with the truncated bond terminated through oxygen atoms.[49] Another proposal is that the origin of the satellite features is an energy loss of the Ru 3d photoemitted electrons through plasmon excitation in the RuO_2 film.[50] There are, in addition, authors claiming that the satellites are due to final-state screening effects.[47,51] Final-state screening effects arise from the strong Coulomb interaction between valence electrons and the core hole produced in the photoionization process. A possible change in the

core hole screening from mainly localized *d*-level screening to mainly extended *sp*-band screening result in two different final states, very often denoted well-screened and unscreened, respectively, and subsequently show main lines and satellites as complex features in the XPS spectrum. The phenomenon is general for metallic transition metal components[23] and is the most likely explanation of the observed satellites, especially since the appearance of the satellites are insensitive to the probing depth and, thus, excludes surface induced effects: the Ru 3d spectra in Figure 6 are obtained with probing depth of 20 and 70 Å for part (a) and (b), respectively. Even though the origin of the satellite features is not yet unambiguously verified, the conclusions of our work are independent of their presence in the Ru 3d spectra.

The Ru 3d XPS spectra of the RuO_2-, mixed $(Ru_{0.5}:Ti_{0.5})O_2$-, and mixed $(Ru_{0.3}:Ti_{0.7})O_2$ coatings are shown in Figure 7 as part (a), (b) and (c), respectively. The Ru 3d spectra of the mixed $(Ru_{1-x}:Ti_x)O_2$ (x = 0.5 and 0.7) coatings have an overall reduced intensity compared to the pure RuO_2 coating, which mainly is due to the lower Ru content. The intensities are, however, not calibrated and for best comparison the spectra in Figure 7 are scaled to have the same intensity at the high binding energy background. The shape of the Ru 3d spectrum of the mixed $(Ru_{1-x}:Ti_x)O_2$ coating changes as the concentration of TiO_2 is varied and a few trends can be observed. The most apparent is the change in the intensity ratio between the Ru $3d_{5/2}$ and $3d_{3/2}$ main peaks. In addition, the peak intensity ratio between the Ru $3d_{5/2}$ main peak and its satellite is decreasing with higher TiO_2 concentration. The change in the shape in the binding energy region 280 – 283 eV can be explained through a partial peak shift, i.e. a part of the Ru $3d_{5/2}$ main peak is shifted toward higher binding energies and into the Ru $3d_{5/2}$ satellite region due to the presence of Ti. Since the shift of the Ru $3d_{5/2}$ is filling up the dip at 281.9 eV, the shift of the main peaks is estimated to be about 0.8 eV. In the Supporting Information the intensity distribution in the

binding energy region 280 – 283 eV is further investigated through peak fitting of the XPS spectra. The result from the peak fitting process corroborates the suggestion of a partial shift of the Ru $3d_{5/2}$ toward higher binding energies.

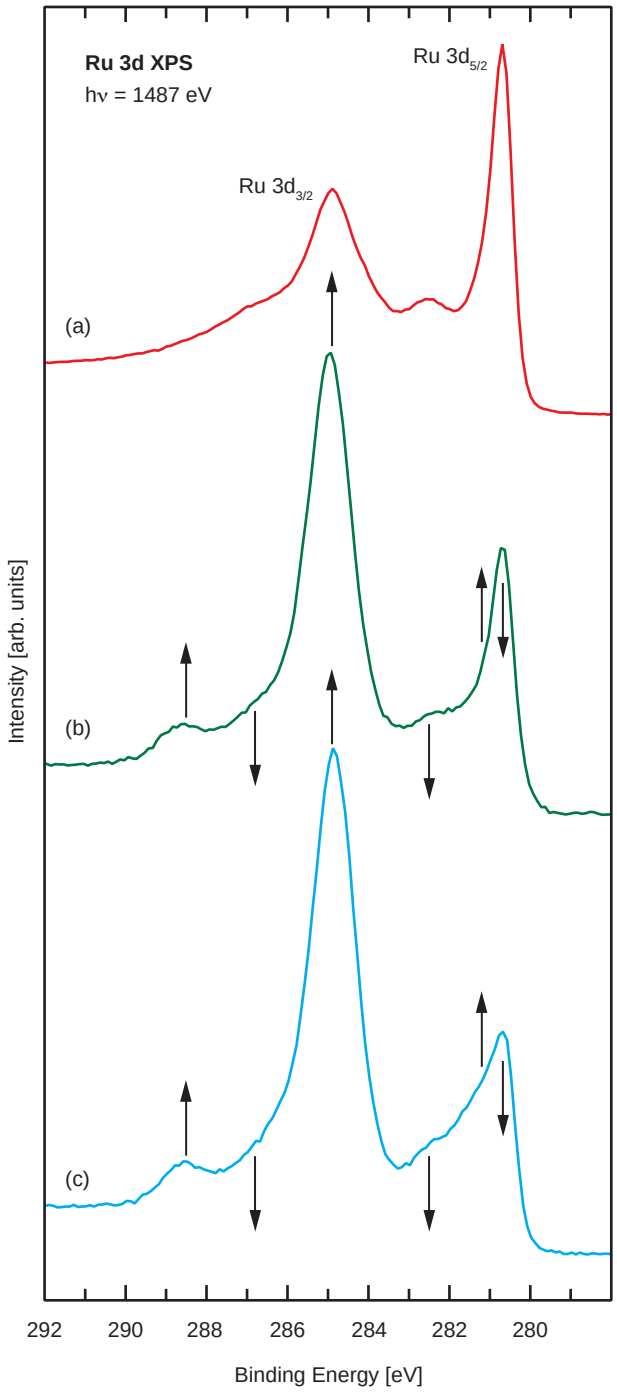

Figure 7. Ru 3d XPS of (a) RuO_2-, (b) mixed $(Ru_{0.5}:Ti_{0.5})O_2$-, and (c) mixed $(Ru_{0.3}:Ti_{0.7})O_2$ coatings obtained through soft X-ray excitation. The arrows indicate the change in intensity when going from (a) to (b) to (c). In the binding energy region 280 – 283 eV it is suggested that the Ru atoms in the mixed $(Ru_{1-x}:Ti_x)O_2$ (x = 0.5 and 0.7) coatings have a part of the $3d_{5/2}$ main peak redistributed toward higher binding energy by in average 0.8 eV, compare to the RuO_2 coating.

The observed changes in intensity above 283 eV indicate a complex and delicate modification of the Ru-components in the coating. However, since the conclusions of our work are independent of the presence of the features above 283 eV we will not speculate about their origin. Nevertheless, a brief discussion is included in the Supporting Information.

The shift toward lower binding energies observed in the Ti 2p spectra of mixed $(Ru_{1-x}:Ti_x)O_2$ coatings (see Figure 5) is, thus, accompanied with a shift toward higher binding energies observed in the corresponding Ru 3d spectra. Hence, the XPS study infers that charge is transferred from the RuO_2 to the TiO_2 in mixed $(Ru_{1-x}:Ti_x)O_2$ coatings. A charge transfer toward the element with the larger fraction of empty states in its valence band is a common observation at surfaces that contain mixtures of two transition metals.[52] However, a charge transfer between Ru and Ti in TiO_2-doped RuO_2 nanoparticle coatings has, as far as we know, not previously been reported in the literature. It has, though, been proposed in an earlier XPS study of RuO_2 adsorption on single crystal Ti(110).[53]

3.3. The benefit of TiO_2-doping on RuO_2 catalyst. The combined SECM and XPS study suggests that charge is transferred from the RuO_2 to the TiO_2, which produces the partial reduction of TiO_2 into $TiO_2^{\delta-}$ and simultaneously the partial oxidation of RuO_2 into $RuO_2^{\delta+}$. In a surface sensitive XPS study Over *et al.*[50] showed that a RuO_3 component at the surface of

RuO_2(110) introduces an intensity increase at 281.8 eV, which is not far from the intensity increase we can observe around 281.5 eV for the $(Ru_{1-x}:Ti_x)O_2$ that we assign to the $RuO_2^{\delta+}$. The charge redistribution, thus, suggests that TiO_2-doping promotes the formation of an activated precursor state, $RuO_2^{\delta+}$, as a preparatory step toward the electrocatalytic process that facilitates water oxidation through the RuO_3 formation and its subsequent decomposition back into RuO_2 and O_2 according to the three main reaction parts represented by (3), (4) and (5):

$$2RuO_2 + 2TiO_2 \rightarrow 2RuO_2^{\delta+} + 2TiO_2^{\delta-} \quad (3)$$

$$2RuO_2^{\delta+} + 2H_2O \rightarrow 2RuO_3 + 4H^+ + 4e^- \quad (4)$$

$$2RuO_3 \rightarrow 2RuO_2 + O_2 \quad (5)$$

Hence, at a significant value of *x* in the mixed $(Ru_{1-x}:Ti_x)O_2$ coatings the charge transfer is substantial enough to benefit the electrocatalytic activity for water oxidation in acidic media. The improved electrocatalytic activity is further enhanced at larger values of *x*, due to a more effective charge transfer, which corroborates earlier studies that showed that no improvement in the electrocatalytic activity is obtained for mixed $(Ru_{1-x}:Ti_x)O_2$ coatings with $x < 0.7$.[10]

The formation of $RuO_2^{\delta+}$, i.e. the loss of charge from the surface RuO_2, is evenly distributed due to the mixed-in TiO_2 that work as a charge reservoir and the OER is, thus, promoted uniformly over the surface, as shown on the left side of the SECM image in Figure 1. On the right side in the SECM image of Figure 1 the pure RuO_2 coating, on the other hand, shows surface regions that are less electrocatalytically active separated by high OER activity at cracks and at the border to the TiO_2 film. The non-uniform activity on the pure RuO_2 coating is due to the fact that the pure RuO_2 coating is applied on a Ti substrate and the acidic nature of the

precursor solution causes diffusion of Ti into the coating that form TiO_2-doped RuO_2 near the substrate. Since the pure RuO_2 coating has cracks that penetrate down to the TiO_2-doped RuO_2 near the substrate, an enhanced electrocatalytic activity will occur in the bottom of the cracks. Since the resolution of the SECM image is set by the size of the UME-tip, which is much larger than the width of the cracks, the enhanced electrocatalytic activity in the cracks will appear as highly active areas on the pure RuO_2 coating. On the TiO_2-doped RuO_2 coating, on the other hand, the evenly distribution of the TiO_2 in the coating results in a uniform electrocatalytic activity over the whole surface. For the same reason, i.e. diffusion of Ti into the coating, the border between the pure RuO_2 and the TiO_2 film shows an increased electrocatalytic activity while the border between the TiO_2-doped RuO_2 and the TiO_2 film shows the opposite effect.

An alternative explanation to the enhanced OER activity in the mixed $(Ru_{1-x}:Ti_x)O_2$ coatings has, however, recently been presented in the literature. The study, which was based on density functional theory calculations, compared the required overpotential for the OER activity on un-doped TiO_2(110) and doped rutile M-TiO_2(110), where *M* is a transition metal. In this theoretical analysis Garcia-Mota *et al.*[37] found a considerable enhanced OER activity on the M-TiO_2 (M= Cr, Mo, Mn, or Ir) compare to pure TiO_2, although, the study did not demonstrate that M-doped TiO_2 would provide a better OER activity than pure RuO_2.

4. CONCLUSIONS

The SECM SG/TC image obtained using a gold UME tip for sensing the electrochemical activity for water oxidation reaction, i.e. the O_2 evolution produced on DSA® type electrodes such as pure RuO_2 and TiO_2-doped RuO_2 coated electrodes, shows an average higher current on the mixed $(Ru_{1-x}:Ti_x)O_2$ coated (Ru:Ti, surface composition ≈ 50:50) compare to the pure RuO_2

coated electrode. In addition, the TiO_2-doped RuO_2 coated electrode exhibits a more evenly distributed electrocatalytic activity for water oxidation compared to the pure RuO_2 coated electrode. Furthermore, the comparison between the optical microscope and the SECM images, on the same pure RuO_2 coated electrode, correlated regions of higher electrocatalytic activity with observed crack pattern. The higher electrochemical activity at the cracks, successfully demonstrated through the SG/TC mode of the SECM, is probably because of TiO_2-doping in the first applied layer of RuO_2 due to Ti diffusion from the Ti sheet acting as a support.

X-ray photoelectron spectroscopy suggests that the electrocatalytic enhancement for OER on the mixed $(Ru_{1-x}:Ti_x)O_2$ coating is promoted through a charge transfer from the RuO_2 to the TiO_2, which provides new and more reactive sites designated as activated $RuO_2^{\delta+}$, as indicated through the shifts of the Ti 2p and Ru 3d toward lower and higher binding energies, respectively. The observation further indicates that the quantity of RuO_2 present in mixed $(Ru_{1-x}:Ti_x)O_2$ coatings controls the amount of the charge transfer.

In conclusion, we provide here additional and valuable insight into the mechanism of electrocatalytic water oxidation on industrially relevant $(Ru_{1-x}:Ti_x)O_2$ DSA® type electrodes. We can conclude from the combined SECM and XPS study that, even though the Ru content in the mixed $(Ru_{1-x}:Ti_x)O_2$ coating is considerable lower compare to pure RuO_2 coating, the former is more efficient for electrocatalytic water oxidation than the latter. Thus, the TiO_2-doping and particularly the interaction between the Ti and the Ru plays a significant role in enhancing the OER activity on these mixed oxide coated electrodes.

ASSOCIATED CONTENT

Supporting Information

Peak fitting of the XPS spectra has been performed and the result is presented in the Supporting Information. In addition there is also a brief discussion about the origin of the intensity increase that is observed in the XPS spectra above 283 eV for the mixed $(Ru_{1-x}:Ti_x)O_2$ coatings. This material is available free of charge via the Internet at http://pubs.acs.org.

AUTHOR INFORMATION

Corresponding Author

lars-ake.naslund@liu.se

Present Addresses

[#]Department of Applied Science and Design, Mid Sweden University, SE-851 70 Sundsvall, Sweden

Notes

The authors declare no competing financial interest.

ACKNOWLEDGMENT

This study has partly been carried out in the framework of the European Commission FP7 Initial Training Network “ELCAT”, Grant Agreement No. 214936-2. Portions of this research were performed at SPring-8 with the approval of Japan Synchrotron Radiation Research Institute as Nanotechnology Support Project of the Ministry of Education, Culture, Sports, Science and Technology (Proposal No. 2007A2005 and 2008A1671/BL-47XU). L.-Å. N. also acknowledges the assistance from Hirohito Ogasawara while acquiring the HAXPES data at SPring-8.

REFERENCES

(1) Trasatti, S. in *The Electrochemistry of Novel Materials*; Lipkowski, J.; Ross, P. N., Eds.; VCH Publishers: New York, 1994, p. 207.

(2) Trasatti, S. *Electrochim. Acta* **2000**, 45, 2377–2385.

(3) Fang, Y.-H.; Liu, Z.-P. *J. Am. Chem. Soc.* **2010**, 132, 18214-18222.

(4) Chen, Z.; Concepcion, J. J.; Jurss, J. W.; Meyer, T. J. *J. Am. Chem. Soc.* **2009**, 131, 15580-15581.

(5) Slavcheva, E.; Nikolova, V.; Petkova, T.; Lefterova, E.; Dragieva, I.; Vitanov, T.; Budevski, E. *Electrochim. Acta* **2005**, 50, 5444-5448.

(6) Marshall, A. T.; Haverkamp, R. G. *Electrochim. Acta* **2010**, 55, 1978-1984.

(7) Nakagawa, T.; Bjorge, N. S.; Murray, R. W. *J. Am. Chem. Soc.* **2009**, 131, 15578-15579.

(8) Over, H. *Chem. Rev.* **2012**, 112, 3356-3426.

(9) Barison, S.; Barreca, D.; Daolio, S.; Fabrizio, M.; Tondello, E. *J. Mater. Chem.* **2002**, 12, 1511-1518.

(10) Aromaa, J.; Forsén, O. *Electrochim. Acta* **2006**, 51, 6104-6110.

(11) Ma, H.; Liu, C.; Liao, J.; Su, Y.; Xue, X.; Xing, W. *J. Mol. Catal. A: Chem.* **2006**, 247, 7–13.

(12) Jirkovský, J.; Makarova, M.; Krtil, P. *Electrochem. Commun.* **2006**, 8, 1417-1422.

(13) Rossmeisl, J.; Dimitrievski, K.; Siegbahn, P.; Nørskov, J. K. *J. Phys. Chem. C* **2007**, 111, 18821-18823.

(14) Rossmeisl, J.; Qu, Z.-W.; Zhu, H.; Kroes, G.-J.; Nørskov, J. K. *J. Electroanal. Chem.* **2007**, 607, 83-89.

(15) Tsuji, E.; Imanishi, A.; Fukui, K.; Nakato, Y. *Electrochim. Acta* **2011**, 56, 2009-2016.

(16) Lyons, M. E. G.; Floquet, S. *Phys. Chem. Chem. Phys.* **2011**, 13, 5314–5335.

(17) Cruz, J. C.; Baglio, V.; Siracusano, S. Antonucci, V.; Aricò, A. S.; Ornelas, R.; Ortiz-Frade, L.; Osorio-Monreal, G.; Durón-Torres, S. M.; Arriaga L. G. *Int. J. Electrochem. Sci.* **2011**, 6, 6607-6619.

(18) Trasati, S. in *Electrodes of Conductive Metallic Oxides, Part B*; Trassati, S. Ed.; Elsevier: Amsterdam, 1980.

(19) Mink, J.; Kristóf, J.; De Battisti, A.; Daolio, S.; Németh, Cs. *Surf. Sci.* **1995**, 335, 252-257.

(20) Kristóf, J.; Daolio, S.; Piccirillo, C.; Facchin, B.; Mink, J. *Surf. Sci.* **1996**, 348, 287-298.

(21) da Silva, L. A.; Alves, V. A.; da Silva, M. A. P.; Trasatti, S.; Boodts, J. F. C. *Can. J. Chem.* **1997**, 75, 1483-1493.

(22) *Scanning Electrochemical Microscopy*; Bard, A. J.; Mirkin, M. V. Eds.; Marcel Dekker: New York, 2001.

(23) Hüfner, S. *Photoelectron spectroscopy: principles and applications*, 3rd ed.; Springer-Verlag: Berlin, Heidelberg, 2010.

(24) Sanchez-Sanchez, C. M.; Solla-Gullon, J.; Vidal-Iglesias, F. J.; Aldaz, A.; Montiel, V.; Herrero, E. *J. Am. Chem. Soc.* **2010**, 132, 5622-5624.

(25) Sanchez-Sanchez, C. M.; Vidal-Iglesias, F. J.; Solla-Gullon, J.; Montiel, V.; Aldaz, A.; Feliu, J. M.; Herrero, E. *Electrochim. Acta* **2010**, 55, 8252-8257.

(26) Minguzzi, A.; Alpuche-Aviles, M. A.; Rodriguez-López, J.; Rondinini, S.; Bard, A. J. *Anal. Chem.* **2008**, 80, 4055-4064.

(27) Sanchez-Sanchez, C. M.; Rodriguez-Lopez, J.; Bard, A. J. *Anal. Chem.* **2008**, 80, 3254-3260.

(28) Zeradjanin, A. R.; Schilling, T.; Seisel, S.; Bron, M.; Schuhmann, W. *Anal. Chem.* **2011**, 83, 7645-4650.

(29) Wittstock, G.; Burchardt, M.; Pust, S. E.; Shen, Y.; Zhao, C. *Angew. Chem., Int. Ed.* **2007**, 46, 1584-1617.

(30) Bertoncello, P. *Energy Environ. Sci.* **2010**, 3, 1620-1633.

(31) Lin, C.-L.; Sánchez-Sánchez, C. M.; Bard, A.J. *Electrochem. Solid-State Lett.* **2008**, 11, B136-B139.

(32) Malmgren, C.; Hummelgård, M.; Bäckström, J.; Cornell, A.; Olin, H. *J. Phys. Conf. Ser.* **2008**, 100, 052026.

(33) Klug, H. P.; Alexander, L. E. *X-ray Diffraction Procedures*, 2nd ed.; Wiley: New York, 1974.

(34) Malmgren, C.; Eriksson, A. K.; Cornell, A.; Bäckström, J.; Eriksson, S.; Olin, H. *Thin Solid Films* **2010**, 518, 3615–3618.

(35) National Institute of Standards and Technology, Electron Inelastic-Mean-Free-Path Database 1.1, http://www.nist.gov/srd/nist71.htm.

(36) Tanuma, S.; Powell, C. J.; Penn, D. R. *Surf. Interface Anal.* **2011**, 43, 689-713.

(37) Garcia-Mota, M.; Vojvodic, A.; Metiu, H.; Man, I. C.; Su, H. Y.; Rossmeisl, J.; Norskov, J. K. *ChemCatChem* **2011**, 3, 1607-1611.

(38) Sathish, M.; Viswanathan, B.; Viswanath, R. P.; Gopinath, C. S. *Chem. Mater.* **2005**, 17, 6349-6353.

(39) Takahashi, I.; Payne, D. J.; Palgrave, R. G.; Egdell, R. G. *Chem. Phys. Lett.* **2008**, 454, 314-317.

(30) Nambu, A.; Graciani, J.; Rodriguez, J. A.; Wu, Q.; Fujita, E.; Fdez Sanz, J. *J. Chem. Phys.* **2006**, 125, 094706.

(41) Gouttebaron, R.; Cornelissen, D.; Snyders, R.; Dauchot, J. P.; Wautelet, M.; Hecq, M. *Surf. Interface Anal.* **2000**, 30, 527–530.

(42) Okazaki, K.; Ichikawa, S.; Maeda, Y.; Haruta, M.; Kohyama, M. *Appl. Catal. A* **2005**, 291, 45-54.

(43) Chan, H. Y. H.; Takoudis, C. G.; Weavery, M. J. *J. Catal.* **1997**, 172, 336-345.

(44) Rochefort, D.; Dabo, P.; Guay, D.; Sherwood, P. M. A. *Electrochim. Acta* **2003**, 48, 4245-4252.

(45) Bhaskar, S.; Dobal, P. S.; Majumder, S. B.; Katiyar, R. S. *J. Appl. Phys.* **2001**, 89, 2987-2992.

(46) Petrykin, V.; Bastl, Z.; Franc, J.; Macounova, K.; Makarova, M.; Mukerjee, S.; Ramaswamy, N.; Spirovova, I.; Krtil, P. *J. Phys. Chem. C* **2009**, 113, 21657–21666.

(47) Kim, Y. J.; Gao, Y.; Chambers, S. A. *Appl. Surf. Sci.* **1997**, 120, 250-260.

(48) Mårtensson, N.; Nyholm, R. *Phys. Rev. B* **1981**, 24, 7121.

(49) Reuter, K.; Scheffler, M. *Surf. Sci.* **2001**, 490, 20-28.

(50) Over H.; Seitsonen, A. P.; Lundgren, E.; Smedh, M.; Andersen, J. N. *Surf. Sci.* **2002**, 504, L196–L200.

(51) Cox, P. A.; Goodenough, J. B.; Tavener, P. J.; Telles, D. *J. Solid State Chem.* **1986**, 62, 360-370.

(52) Rodriguez, J. A.; Goodman, D. W. *Science*, **1992**, 257, 897-903.

(53) Rizzi, G. A.; Magrin, A.; Granozzi, G. *Surf. Sci.* **1999**, 443, 277-286.

Table of Contents artwork